Publications

Available Online

J. Sci. Res. **18** (1), 167-186 (2026)

JOURNAL OF SCIENTIFIC RESEARCH

www.banglajol.info/index.php/JSR

A DFT Study of the Geometrical, Electronic, Optical, Spectroscopic and Wave Function Analyses (ESP, ELF, LOL) of 8-Hydroxy Coumarin: A Molecule with Large Medicinal Applications

Sabyasachi Khatua*

Department of Chemistry, Y S Palpara Mahavidyalaya, Palpara-721458, West Bengal, India

Received 24 April 2025, accepted in final revised form 11 October 2025

Abstract

A comprehensive theoretical investigation of 8-hydroxy coumarin has been conducted to elucidate its geometrical, spectroscopic, and electronic properties. Geometrical analysis reveals the impact of the carbonyl and hydroxyl groups on bond lengths and bond angles. This is supported by consistent findings from Laplacian of electron density ($\nabla^2\rho$) calculations. Natural Bond Orbital (NBO) analysis highlights significant conjugative and hyper-conjugative interactions that enhance molecular stability. Time-Dependent Density Functional Theory (TD-DFT) calculations identify a HOMO-LUMO energy gap of 4.32 eV, while simulated UV spectra feature sharp peaks at 220 nm and 289 nm, along with a small shoulder between 215–240 nm. Simulated Infrared (IR) and Nuclear Magnetic Resonance (NMR) spectra align well with experimental data. The electronic structure of 8-OH coumarin is explored through Electron Localization Function (ELF) and Localized Orbital Locator (LOL) studies. Density of States (DOS) studies unveils bonding, non-bonding, and antibonding interactions. Nonlinear optical (NLO) analysis reveals significant optical activity, while Reduced Density Gradient (RDG) analysis excludes intramolecular hydrogen bonding but indicates weak van der Waals and steric interactions.

Keywords: Time-Dependent Density Functional Theory; Natural Bond Orbital; Electron Localization Function; Localized Orbital Locator; Density of States.

doi: https://dx.doi.org/10.3329/jsr.v18i1.81170 J. Sci. Res. **18** (1), 167-186 (2026)

1. Introduction

Coumarin-based compounds are widely recognized as a vital family of organic heterocyclic compounds. *Dipteryx odorata* is a tree of the pea family. Its seeds are known as tonka beans. The term *coumarin* originates from the French word *coumarou*, referring to the tonka bean. It was obtained as a natural compound for the first time in 1820 from *Dipteryx odorata* [1]. Apart from tonka beans, coumarins naturally occur in a wide range of plants, including lavender, strawberries, apricots, cherries, cinnamon, and bison grass [2]. They are extensively used in various fields of science, technology and everyday life [3]**.** Coumarin and its various derivatives have a wide range of medicinal applications. They are known to

---

* *Corresponding author:* skhatua1@gmail.com

have anti-inflammatory [4,5], anti-oxidant [6], anti-thrombotic, anti-allergic [7], hepato-protective, anti-viral [8,9] and anti-carcinogenic activities [10]. Warfarin is a well-known coumarin derivative which functions as an effective blood thinner and rat poison [11]. In everyday life also they have versatile applications in the form of cosmetics, insecticides, food preservatives, optical brightening agents and fluorescent laser dyes [12–14]

Due to such wide range of applications, coumarin and its derivatives have gained significant attention in recent years [15–19]. In a previous investigation Huong *et al*. [18] have examined the influence of hydroxyl group positioning on the antioxidant activity of coumarin derivatives. While most research has primarily focused on their medicinal potential, comparatively few studies have addressed the electronic and spectroscopic properties of these compounds [17,19]. The study of electronic properties is of particular importance, as they play an important role in rational drug design. Notably, no systematic investigation has been reported on the effect of hydroxyl substitution at the 8th position of coumarin. The present work is therefore novel as it aims to fill this gap by providing the first comprehensive analysis of the spectroscopic and electronic properties of 8-hydroxy coumarin through Density Functional Theory (DFT) calculations.

2. Computational Methods

Gas-phase calculations were conducted using the Gaussian 09 software package [20] under the Density Functional Theory (DFT) formalism and GaussView [21] served as the molecular visualization tool. Geometry optimization of the title compound is done using B3LYP model using 6-311++G(d,p) basis set. Multiwfn package [22] was utilized to explore potential hydrogen bonding in the title compound. Time-Dependent Density Functional Theory (TDDFT) was employed to simulate the UV–Vis spectrum of the geometry optimized at the B3LYP/6-311++G(d,p) level. Gas-phase IR frequencies were obtained using the B3LYP/6-311++G(d,p) computational model. All vibrational assignments and analyses are performed using VEDA 4 software program [23].

3. Results and Discussion

3.1. *Geometrical analysis*

Fig. 1. The optimized structure of 8-OH coumarin.

Gas-phase geometry optimization of 8-OH coumarin was performed using the B3LYP functional in combination with the 6-311++G(d,p) basis set. The optimized geometry of 8-OH coumarin in gas phase is shown in Fig. 1 and the optimized geometrical parameters are presented in Table 1. The ideal C-C bond lengths of benzene rings are approximately 1.39 Å. But in the present study the C2-C3, C3-C4 and C4-C10 bond lengths of the first ring are estimated to be 1.46 Å, 1.35 Å, and 1.44 Å, respectively. This clearly shows that the carbonyl group presumably has a significant influence on the C-C bond lengths of the title compound. This is further justified from the fact that while moving further from the carbonyl group to the second ring, the influence seems to be almost insignificant. The C-C bond lengths in the second ring varies between 1.39 Å and 1.41 Å, which are very close to the ideal C-C bond length. The C7-C8 and C8-C9 bond lengths of the second ring are calculated to be 1.39 Å and 1.40 Å respectively. This suggests that the hydroxyl group exerts a significantly weaker effect on the C–C bond length as compared to the carbonyl group.

Table 1. Optimized structural parameters of 8-OH coumarin.

Name	Definition	Value
Bond length (Å)		
R1	O_1-C_2	1.4018
R2	O_1-C_9	1.3689
R3	C_2-C_3	1.4572
R4	C_2-O_{12}	1.2013
R5	C_3-C_4	1.3509
R6	C_3-H_{13}	1.0815
R7	C_4-C_{10}	1.4406
R8	C_4-H_{14}	1.0853
R9	C_5-C_6	1.3862
R10	C_5-C_{10}	1.4065
R11	C_5-H_{15}	1.0836
R12	C_6-C_7	1.3995
R13	C_6-H_{16}	1.0832
R14	C_7-C_8	1.3901
R15	C_7-H_{17}	1.0831
R16	C_8-C_9	1.4005
R17	C_8-O_{11}	1.3575
R18	C_9-C_{10}	1.3989
R19	O_{11}-H_{18}	0.9674
Bond angle (^{0})		
A1	C_2-O_1-C_9	122.5075
A2	O_1-C_2-C_3	115.4059
A3	O_1-C_2-O_{12}	117.7065
A4	C_3-C_2-O_{12}	126.8876
A5	C_2-C_3-C_4	122.0379
A6	C_2-C_3-H_{13}	115.3895
A7	C_4-C_3-H_{13}	122.5726
A8	C_3-C_4-C_{10}	121.1764
A9	C_3-C_4-H_{14}	120.2067
A10	C_{10}-C_4-H_{14}	118.6169
A11	C_6-C_5-C_{10}	119.691
A12	C_6-C_5-H_{15}	120.8887

A13	C_{10}-C_{5}-H_{15}	119.4203
A14	C_{5}-C_{6}-C_{7}	120.8844
A15	C_{5}-C_{6}-H_{16}	119.9571
A16	C_{7}-C_{6}-H_{16}	19.1584
A17	C_{6}-C_{7}-C_{8}	120.3185
A18	C_{6}-C_{7}-H_{17}	121.17
A19	C_{8}-C_{7}-H_{17}	118.5115
A20	C_{7}-C_{8}-C_{9}	118.6005
A21	C_{7}-C_{8}-O_{11}	120.2701
A22	C_{9}-C_{8}-O_{11}	121.1294
A23	O_{1}-C_{9}-C_{8}	115.9908
A24	O_{1}-C_{9}-C_{10}	122.2989
A25	C_{8}-C_{9}-C_{10}	121.7104
A26	C_{4}-C_{10}-C_{5}	124.6315
A27	C_{4}-C_{10}-C_{9}	116.5734
A28	C_{5}-C_{10}-C_{9}	118.7951
A29	C_{8}-O_{11}-H_{18}	108.8559

The same kind of influence of the substituents is also observed in case of internal CCC bond angles of the title compound. The O1-C2-C3 and C4-C10-C9 bond angles of the first ring are calculated as 115.41° and 116.57° respectively. The remaining CCC bond angles of the first ring vary approximately between 121° and 122°. On the contrary, C7-C8-C9, C8-C9-C10 and C5-C10-C9 bond angles of the second ring are estimated to be 118.60°, 121.71° and 118.80° respectively. The remaining CCC bond angles are very close to the ideal value of 120°. This indicates that the deviations from the ideal value are more pronounced near the point of attachment of the substituents, namely the carbonyl group and the hydroxyl group. So, the aromatic ring of the title compound is perturbed to some extent and the symmetry of the ring is lowered.

3.2. *Topological analysis*

Fig. 2 shows all (3, -1) Bond Critical Points (BCP) present in the title compound. All BCPs lie approximately in the middle of the bond. No bond path is observed between O_1 and H_{39}. This clearly indicates that there is virtually no hydrogen bonding interaction. This observation is further supported by the Natural Bond Orbital (NBO) analysis. The electron density (ρ) and the Laplacian of electron density ($\nabla^2\rho$) at the BCP of all bonds are listed in Table 2.

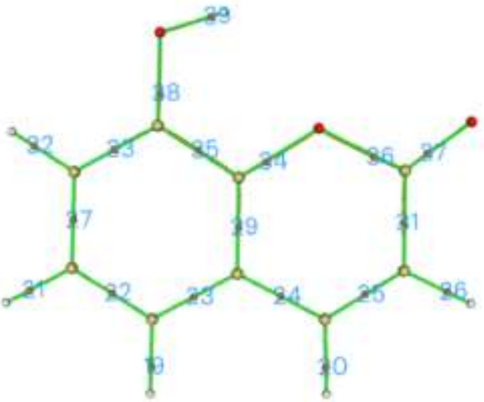

Fig. 2. (3, -1) BCPs of 8-OH coumarin.

Table 2. The electron density (ρ) and Laplacian of electron density ($\nabla^2\rho$) of all the BCPs in a.u.

Bonds	Density of all electrons (ρ)	Laplacian of electron density ($\nabla^2\rho$)
O_1-C_2	0.25888	-0.41535
O_1-C_9	0.27500	-0.23088
C_2-C_3	0.28026	-0.73853
C_2-O_{12}	0.42426	-0.19911
C_3-C_4	0.33334	-0.97721
C_4-C_{10}	0.28475	-0.75857
C_5-C_6	0.31246	-0.87571
C_5-C_{10}	0.30047	-0.81779
C_6-C_7	0.30418	-0.83610
C_7-C_8	0.31330	-0.88956
C_8-C_9	0.31175	-0.87881
C_8-O_{11}	0.29083	-0.40256
C_9-C_{10}	0.30848	-0.85982
C_3-H_{13}	0.28373	-0.98415
C_4-H_{14}	0.28303	-0.98415
C_5-H_{15}	0.28116	-0.96380
C_6-H_{16}	0.28254	-0.97540
C_7-H_{17}	0.28199	-0.97231
O_{11}-H_{18}	0.36017	-2.54015

The values of $\nabla^2\rho$ are very useful in interpreting the electronic structure of a molecule [24,25]. All (3, -1) interactions within the title compound are typical open - shell interactions with negative $\nabla^2\rho$ values. It is observed that the topology analysis is very much consistent with the findings of geometrical analysis. The geometrical analysis shows that among the substituents, only carbonyl group has significant influence on the ring structure and that is limited to the first ring only. The same trend is observed in topological analysis also. The electron density predominantly changes along O_1-C_2, O_1-C_9, C_2-O_{12} and C_2-C_3 bonds which are in close proximity with the carbonyl group. But in the second ring, the electron densities of all C-C bonds are virtually constant. Interestingly the variations of the topological properties at the BCPs are consistent with changes in bond lengths.

3.3. *NBO analysis*

The electronic structure and hybridization of the atoms in 8-hydroxycoumarin were examined through NBO calculations.

3.3.1. *Natural population analysis*

Table 3. Accumulation of natural charges, population of electrons in core, valence and Rydberg orbitals.

Atom No.	Natural Charge (e)	Natural population (e) Core	Valence	Rydberg	Total (e)
O_1	-0.54239	1.99967	6.52430	0.01842	8.54239
C_2	0.75372	1.99925	3.20161	0.04542	5.24628
C_3	-0.30082	1.99904	4.28519	0.01660	6.30082
C_4	-0.10374	1.99909	4.08684	0.01781	6.10374
C_5	-0.19077	1.99910	4.17497	0.01669	6.19077
C_6	-0.19516	1.99918	4.17883	0.01715	6.19516
C_7	-0.22265	1.99909	4.20617	0.01739	6.22265
C_8	0.28851	1.99871	3.68711	0.02567	5.71149
C_9	0.28673	1.99865	3.69321	0.02141	5.71327
C_{10}	-0.13453	1.99896	4.11953	0.01604	6.13453
O_{11}	-0.66341	1.99975	6.65095	0.01271	8.66341
O_{12}	-0.55285	1.99974	6.54001	0.01311	8.55285
H_{13}	0.23091	0.00000	0.76738	0.00171	0.76909
H_{14}	0.21380	0.00000	0.78446	0.00174	0.78620
H_{15}	0.20885	0.00000	0.78863	0.00252	0.79115
H_{16}	0.21117	0.00000	0.78710	0.00173	0.78883
H_{17}	0.22282	0.00000	0.77531	0.00186	0.77718
H_{18}	0.48981	0.00000	0.50552	0.00467	0.51019

The B3LYP/6-311++G(d,p) optimized geometry of 8-hydroxy coumarin was subjected to natural population analysis [26]. The results, including atomic charge distribution and electron population in the core, valence, and Rydberg sub-shells, are summarized in Table 3. The most electropositive charge (0.75372) is accumulated on C_2 atom. Also, atoms C_8 and C_9 have acquired small positive charges. On the other hand, the most electronegative charges are centred on the three oxygen atoms. All the other carbon atoms of both rings have negative charges, although the amount of negative charge is not uniform. This indicates that the delocalization is not uniform throughout the rings. Presumably this is due to the presence of the carbonyl and hydroxyl groups. The distribution of electrons in various sub-shells is shown in Table 4.

Table 4. Percentage of distribution of electrons in core, valence and Rydberg orbitals.

Core	23.99023 (99.9593 % of 24)
Valence	59.75711 (99.5952 % of 60)
Rydberg	0.25265 (0.3008 % of 84)

3.3.2. *Natural bond orbital (NBO) analysis*

NBO analysis [27,28] provides insight into electron delocalization by describing the transfer of electron density from filled Lewis-type orbitals, such as bonding or lone pairs, into unoccupied non-Lewis orbitals including anti-bonding and Rydberg functions. Results of NBO analysis are summarized in Table 5. The analysis highlights the dominant NBO interactions and reports the corresponding second-order perturbation energies, also recognized as stabilization or interaction energies. The compound gains stability through various conjugative and hyper-conjugative interactions. Interestingly the strongest interaction is $\pi^* \ (C_9 - C_{10}) \rightarrow \pi^* \ (C_5 - C_6)$ with stabilization energy of 208.45 kcal/mol. This is followed by $\pi^* \ (C_2 - O_{12}) \rightarrow \pi^* \ (C_3 - C_4)$ interaction with stabilization energy of 128.75 kcal/mol.

Table 5. Second order perturbation analysis of the interactions between donor and acceptor orbitals

Donor NBO (i)	Acceptor NBO (j)	E(2) kcal/mol
π (C_2 - O_{12})	π^* (C_3 – C_4)	5.27
π (C_3 – C_4)	π^* (C_2 - O_{12})	22.12
π (C_3 – C_4)	π^* (C_9 – C_{10})	11.26
σ (C_3 – H_{13})	σ^* (O_1 – C_2)	4.47
σ (C_3 – H_{13})	σ^* (C_4 – C_{10})	4.50
σ (C_4 – H_{14})	σ^* (C_2 – C_3)	4.32
π (C_5 – C_6)	π^* (C_7 – C_8)	18.33
π (C_5 – C_6)	π^* (C_9 – C_{10})	19.77
σ (C_5 – C_{10})	σ^* (O_1 – C_9)	4.10
σ (C_5 – H_{15})	σ^* (C_9 – C_{10})	4.17
σ (C_6 – C_7)	σ^* (C_8 - O_{11})	4.14
π (C_7 – C_8)	π^* (C_5 – C_6)	20.05
π (C_7 – C_8)	π^* (C_9 – C_{10})	20.52
σ (C_8 – C_9)	σ^* (C_9 – C_{10})	4.43
σ (C_9 – C_{10})	σ^* (C_8 – C_9)	4.44
π (C_9 – C_{10})	π^* (C_3 – C_4)	15.07
π (C_9 – C_{10})	π^* (C_5 – C_6)	16.72
π (C_9 – C_{10})	π^* (C_7 – C_8)	19.14
σ (O_{11} – H_{18})	σ^* (C_7 – C_8)	4.81
n_1 O_1	σ^* (C_2 – C_3)	4.15
n_1 O_1	σ^* (C_9 – C_{10})	6.00
n_2 O_1	π^* (C_2 - O_{12})	32.41
n_2 O_1	π^* (C_9 – C_{10})	26.52
n_1 O_{11}	σ^* (C_8 – C_9)	5.69
n_2 O_{11}	π^* (C_7 – C_8)	28.61
n_2 O_{12}	σ^* (O_1 – C_2)	39.26
n_2 O_{12}	σ^* (C_2 – C_3)	15.86
σ * (O_1 – C_2)	σ^* (O_1 – C_9)	13.62
π * (C_2 - O_{12})	π^* (C_3 – C_4)	128.75
π * (C_9 – C_{10})	π^* (C_5 – C_6)	208.45

3.4. ***Frontier molecular orbital analysis***

The difference in energy between LUMO and HOMO states provides useful information about charge transfer, stability and intrinsic reactivity of the compound [29–31]. A reduced energy gap facilitates electron transfer processes with greater ease. The HOMO and LUMO orbitals of 8-OH coumarin are shown in Figs. 3 and 4 respectively at an isovalue of 0.02. In these visual representations, negative charge is depicted in red, while positive charge is illustrated in green.

Fig. 3. HOMO

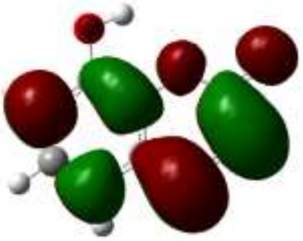

Fig. 4. LUMO

In the HOMO orbital electron density is mainly localized on the second phenyl ring containing the hydroxyl group. For the LUMO orbital, the charge distribution extends throughout the molecular framework. The HOMO is located at −0.24722 a.u. and the LUMO at −0.08874 a.u., corresponding to an estimated gap of 4.32 eV. The simulated UV spectrum is shown in Fig. 5. It shows two sharp peaks at 220 nm and 289 nm and a small shoulder between 215 and 240 nm. The absorption band observed at 220 nm is mainly attributed to HOMO → LUMO+2 and HOMO–1 → LUMO+1 electronic transitions, while the weak shoulder in this region arises from the HOMO → LUMO+1 transition. A second intense peak at 289 nm is associated with the HOMO–1 → LUMO transition. The oscillator strengths and the maximum orbital contributions of these transitions are shown in Table 6. Schematic diagrams of these transitions with the corresponding energies are shown in Fig. 6.

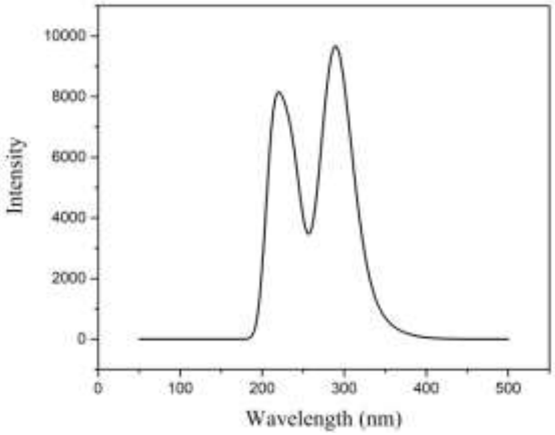

Fig. 5. Simulated UV-visible spectrum of 8-OH coumarin in the gas phase.

Table 6. Vertical excitations with band positions and oscillator strength (f).

Calculated peak (nm)	Oscillator strength	Transition	Max. Orbital Contribution (%)
212.36	0.0923	HOMO → LUMO+2	46.81
218.40	0.0778	HOMO-1 → LUMO+1	49.14
236.96	0.1296	HOMO → LUMO+1	51.58
289.25	0.2368	HOMO-1 → LUMO	91.98

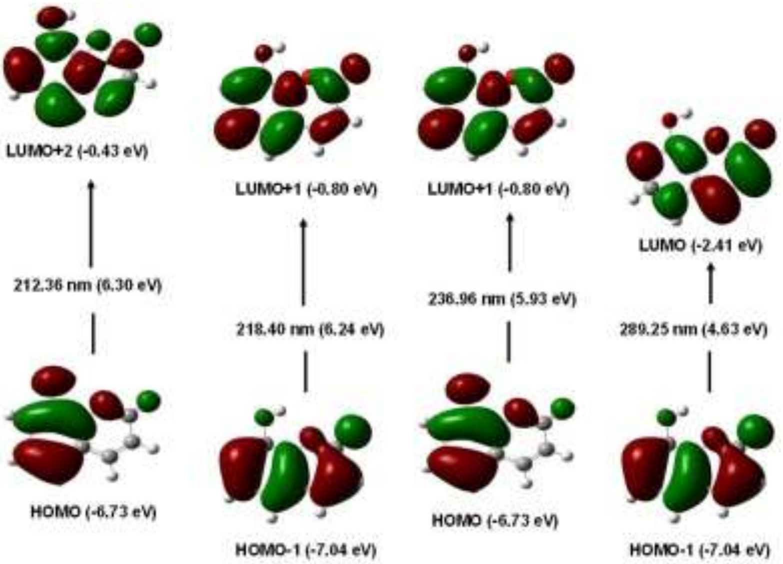

Fig. 6. Schematic representation of vertical excitations of 8-OH coumarin.

3.5. *Vibrational analysis*

The infrared spectrum of 8-OH coumarin is simulated in the gas phase using the DFT/B3LYP/6-311++G(d,p) method. The simulated IR spectrum is shown in Figures 8. Based on the analysis carried out with VEDA 4, all vibrational modes have been assigned. The detailed assignments together with the respective PED values (indicated in parentheses) are provided in Table 7. The absence of any imaginary frequency confirms that the structure corresponds to a genuine minimum on the potential energy surface. The different types of vibrational frequencies are discussed below.

Table 7. Calculated gas phase vibrational frequencies of 8-hydroxy coumarin with probable assignments.

Mode no.	Intensity	Calculated gas phase frequency (cm^{-1})	Vibrational assignments with % PED
1	90.04	3772.13	ν_{OH} (100)
2	0.22	3216.95	ν_{CH} (97)
3	4.38	3201.62	ν_{CH} (93)
4	9.35	3190.46	$\nu_{CH\ asym}$ (97)

5	2.10	3177.77	ν_{CH} (92)
6	5.89	3170.26	ν_{CH} (95)
7	729.97	1809.02	ν_{OC} (84)
8	29.98	1661.53	ν_{CC} (63)
9	39.16	1649.34	$\nu_{CC\,asym}$ (57)
10	134.20	1612.40	ν_{CC} (54)
11	8.59	1518.25	β_{HCC} (11) β_{HCC} (17) β_{HCC} (10)
12	130.15	1487.15	ν_{CC} (21) $\nu_{CC\,asym}$ (17) β_{HCC} (16)
13	21.96	1430.49	β_{HCC} (62)
14	9.38	1403.52	ν_{CC} (36) β_{HOC} (23)
15	15.81	1326.43	ν_{CC} (45) β_{HCC} (22)
16	99.27	1292.38	ν_{CC} (14) $\nu_{OC\,asym}$ (11) β_{HOC} (11) β_{HCC} (12)
17	40.68	1263.02	ν_{OC} (11) β_{HCC} (34) β_{CCC} (11) β_{CCC} (11)
18	106.52	1226.58	$\nu_{CC\,asym}$ (11) ν_{CC} (10) β_{HOC} (32) β_{HCC} (20)
19	15.86	1195.68	β_{HCC} (51)
20	5.86	1177.54	β_{HCC} (44) β_{CCC} (10)
21	61.50	1116.27	ν_{OC} (14) β_{HCC} (13) β_{OCO} (10) β_{CCC} (10)
22	36.38	1083.34	ν_{CC} (44) β_{HCC} (14)
23	59.06	1051.11	ν_{CC} (17) $\nu_{OC\,asym}$ (10) $\nu_{OC\,asym}$ (10) β_{HCC} (10)
24	0.37	1007.79	τ_{HCCC} (87)
25	0.63	968.97	τ_{HCCC} (82)
26	55.15	920.93	$\nu_{OC\,asym}$ (19) β_{CCC} (23) β_{CCC} (10)
27	0.14	899.38	τ_{HCCC} (80)
28	65.98	844.36	τ_{HCCC} (63) δ_{OCCC} (18)
29	27.52	837.89	ν_{OC} (11) β_{CCC} (34)
30	14.58	783.65	τ_{HCCC} (59) δ_{OCCC} (19)
31	0.52	746.85	ν_{CC} (10) β_{CCC} (28) β_{CCC} (13)
32	29.56	733.31	τ_{HCCC} (18) δ_{OCCC} (63)
33	21.58	700.65	ν_{OC} (26) ν_{OC} (10) β_{OCO} (13) β_{COC} (11)
34	2.09	700.52	τ_{HCCC} (14) δ_{OCCC} (61)
35	4.66	574.06	β_{OCO} (47) β_{COC} (14)
36	0.12	573.34	δ_{OCCC} (72)
37	4.29	535.91	τ_{HCCC} (11) τ_{CCCC} (10) τ_{COCC} (12) τ_{CCCC} (51)
38	10.53	533.57	ν_{CC} (11) β_{CCC} (11) β_{CCC} (34)
39	7.83	517.72	β_{CCC} (10) β_{CCO} (42)
40	112.76	452.41	τ_{HOCC} (93)
41	1.01	436.31	ν_{OC} (17) β_{CCC} (51)
42	0.92	420.99	β_{COC} (72)
43	0.48	380.75	τ_{CCCC} (74)
44	0.55	303.98	τ_{CCCC} (63) τ_{COCC} (17) τ_{CCCC} (10)
45	4.38	228.83	β_{CCO} (62)
46	0.69	210.59	τ_{CCCC} (58) τ_{COCC} (10)
47	2.10	140.76	τ_{CCCC} (15) τ_{CCCC} (34) τ_{CCCC} (10)
48	2.05	90.10	τ_{CCCC} (16) τ_{COCC} (46)

3.5.1. *Skeletal vibration*

The bands at 1662, 1612, 1404, 1326, 1292, 1083 and 1051 cm^{-1} are assigned to various aromatic ring C-C symmetric stretching vibrations. Similarly, the bands observed at 1649, 1487 and 1227 cm^{-1} are assigned to various aromatic ring C-C asymmetric stretching vibrations. The bands at 1263, 1178, 1116, 921, 838, 747, 534, 518 and 436 cm^{-1} are assigned to the aromatic ring CCC bending vibrations. Among them, the bands observed at 1263, 1116 and 921 cm^{-1} are of medium intensity whereas the remaining CCC bending vibrations have very low intensity. Finally, the bands observed at 536, 381, 340, 304, 211, 141 and 90 cm^{-1} are assigned to aromatic ring CCCC torsional vibrations.

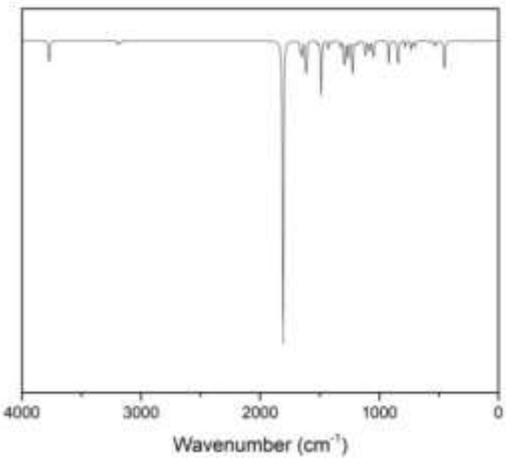

Fig. 7. Simulated IR spectrum of 8-hydroxy coumarin in gas phase.

3.5.2. *C-H vibrations*

The IR bands at 3217 and 3170 cm^{-1} are assigned to C_3-H_{13} and C_4-H_{14} symmetric stretching vibrations and the corresponding PED values are 97 % and 95 % respectively. The band at 3202 cm^{-1} arises from the coupled symmetric stretching vibrations of the three C-H bonds of the second ring with 93 % PED value whereas the band at 3190 cm^{-1} is due to the asymmetric stretching vibration of the same bands. Also, there is another C-H stretching band which appears at 3178 cm^{-1}. The bands observed at 1518, 1487, 1430, 1326, 1292, 1263, 1227, 1196, 1083, 1178, 1116 and 1051 cm^{-1} are assigned to HCC bending vibrations. Finally, the bands observed at 1008, 969, 899, 844, 784, 733, 701 and 536 cm^{-1} are assigned to various HCCC torsional vibrations.

3.5.3. *O-H vibrations*

In organic molecules, O-H stretching vibrations are normally observed in the 3300-3650 cm^{-1} region of the spectrum. But in the present study a very strong O-H stretching band is observed at 3772 cm^{-1} with 100 % PED value. In addition, weak HOC bending vibrations are seen at 1404, 1292 and 1227 cm^{-1}. Further one HOCC torsional vibration is observed at 452 cm^{-1}.

3.5.4. *C-O vibrations*

The C=O stretching modes are normally observed in the 1650-1750 cm^{-1} region of the spectrum. In the present study, one very strong band is observed at 1808 cm^{-1} which is attributed to the stretching mode of the C=O bond. The other C-O stretching modes are seen at 1292, 1263, 1116, 1051, 921, 838 and 701 cm^{-1}. Some bands with moderate intensity are observed at 518 and 229 cm^{-1} which are due to CCO bending vibrations. The COC bending vibrations are seen at 701, 574 and 421 cm^{-1}. Other bands observed at 1116, 701 and 574 cm^{-1} are assigned to OCO bending vibrations. Also, some HOC bending vibrations are seen at 1404, 1292 and 1227 cm^{-1}. The out of plane OCCC vibrations are observed at 844, 784, 733, 701 and 573 cm^{-1}.

3.6. *NMR studies*

Table 8. The experimental and calculated ^{13}C NMR chemical shifts in ppm with respect to TMS.

Atom	Experimental (ppm) [32]	Calculated (ppm)
C_2	160.0	166.7
C_3	116.1	122.4
C_4	144.5	155.9
C_5	118.4	126.9
C_6	124.4	133.0
C_7	118.4	125.4
C_8	144.7	153.2
C_9	142.4	151.8
C_{10}	119.7	127.6
RMSD		8.40

The ^{13}C spectrum of 8-OH coumarin is simulated by GIAO method using B3LYP/6-311++G(d,p) method [33]. All calculations are conducted using polarizable continuum model (PCM) with DMSO as the solvent. All chemical shifts are referenced to tetramethylsilane (TMS). The NMR peaks of TMS are also calculated using the same methods as the title compound. The experimental and simulated chemical shifts are presented in Table 8.

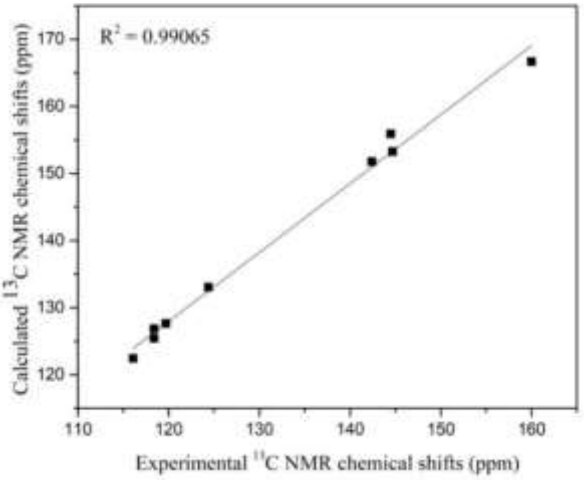

Fig. 8. The linear regression plot between experimental and theoretical ^{13}C NMR chemical shifts.

The position of the NMR peak of an atom depends on the nature of the neighbouring atoms and groups. The ^{13}C NMR shifts of unsaturated carbon atoms of most organic compounds typically varies between 100 and 200 ppm [34]. In the current study, atom C_2 shows maximum chemical shift at 166.7 ppm. Since oxygen is most electronegative among all the atoms of the title compound, C_2 atom, which lies in between two oxygen atoms, is least shielded and it comes into resonance with the external magnetic field at the lowest value. So, the NMR signal of C_2 is maximum down-shifted and the corresponding chemical shift becomes largest. Among the remaining carbon atoms, C_4 shows maximum downfield effect (155.9 ppm), which is closely followed by C_8 (153.2 ppm) and C_9 (151.8 ppm) atoms. The chemical shifts of the remaining carbon atoms do not vary too much. In order to make a correlation between the experimental [32] and simulated data, a linear regression curve is plotted as shown in Fig. 8. The correlation value (R^2) of this plot is 0.99065. This demonstrates that the simulated results are in good agreement with the experimental observations.

3.7. *MEP analysis*

The MEP plot of the title compound is shown in Fig. 9. In this plot red, blue and green colours refer to electron-rich (negative), electron-deficient (positive) and zero electrostatic potential respectively. At an isovalue of 0.02, the electron density values vary from -5.18×10^{-2} a.u. on the negative side to $+5.18 \times 10^{-2}$ a.u. on the positive side. It is obvious that the electron density is localized near the carbonyl group. So, the carbonyl group is more susceptible to electrophilic attack and the electrophile is is anticipated to preferentially attack the oxygen atom of the carbonyl group.

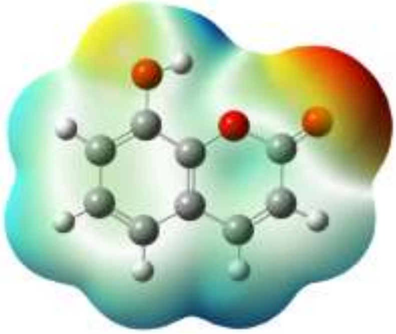

Fig. 9. MEP mapping of 8-OH coumarin.

3.8. *Chemical reactivity studies*

Table 9. Calculated quantum chemical parameters of 8-OH coumarin.

Parameters	Values
Chemical hardness (η)	2.1562 eV
Softness (S)	0.4638 $(eV)^{-1}$
Chemical potential (μ)	-4.5710 eV

Electronegativity (χ)	4.5710 eV
Electrophilicity index (ω)	4.8450 eV
Ionization potential (I)	6.7272 eV
Electron affinity (A)	2.4147 eV

Based on Koopmans's theorem, various parameters related to chemical reactivity can be determined using the following relations.

$$\text{Chemical hardness } (\eta) = \left(\frac{E_{LUMO} - E_{HOMO}}{2}\right)$$

$$\text{Softness } (S) = \frac{1}{\eta} = \left(\frac{1}{E_{LUMO} - E_{HOMO}}\right)$$

$$\text{Chemical potential } (\mu) = \left(\frac{E_{LUMO} + E_{HOMO}}{2}\right)$$

$$\text{Electronegativity } (\chi) = (-\mu) = -\left(\frac{E_{LUMO} + E_{HOMO}}{2}\right)$$

$$\text{Electrophilicity index } (\omega) = \frac{\mu^2}{2\eta}$$

Also, frontier molecular energy values can be used to determine the ionization potential (I) and electron affinity (A) as follows.

$$I = -E_{HOMO}$$
$$A = -E_{LUMO}$$

The ease of charge transfer increases as the energy separation between HOMO and LUMO decreases. As a result, the reactivity will be high and the molecule will exhibit weak stability and more softness. The values of all the parameters discussed above are presented in Table 9.

3.9. *ELF and LOL studies*

Two widely used methods for studying the electronic structure of molecules are Bader's topological analysis of electron density (AIM) [24] and topological analysis of the Electron Localization Function (ELF) [35,36]. ELF offers valuable insights into covalent bond reactivity and electron shell structure [37]. Two-dimensional colour-shaded ELF diagram and the corresponding contour map are displayed in Fig. 10a-b respectively. Fig. 11 shows the ELF shaded surface plot with projection. All ELF diagrams shown in Fig. 10 and 11 are plotted on a scale ranging from 0.0 to 1.0, where red indicates the highest value (1.0) and blue the lowest value (0.0). In this colour scale, values above 0.5 represent bonded and non-bonded localized electrons, whereas values below 0.5 correspond to delocalized electrons [36,38].

The Localized Orbital Locator (LOL) highlights regions of orbital localization where strong overlap produces steep gradients in the localized orbitals [36,38]. The two-dimensional colour-shaded LOL diagram and the corresponding contour map are presented in Fig. 12a-b, respectively. Both diagrams use a colour scale ranging from 0.0 to 1.0. The red areas observed around the hydrogen atoms signify that the electron density has reached the upper limit of the scale, i.e., 1.0. Blue regions surrounding the oxygen and carbon atoms indicate electron delocalization, which is characterized by a depletion of electron density. The red regions between carbon-carbon bonds highlight the covalent nature of these bonds.

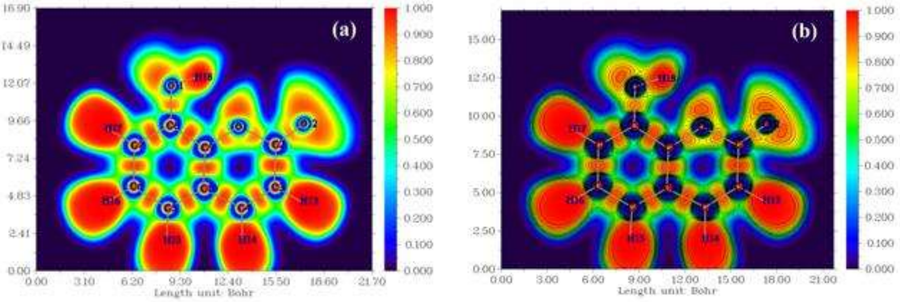

Fig. 10. (a) ELF colour shade diagram and (b) ELF contour map of 8-OH coumarin.

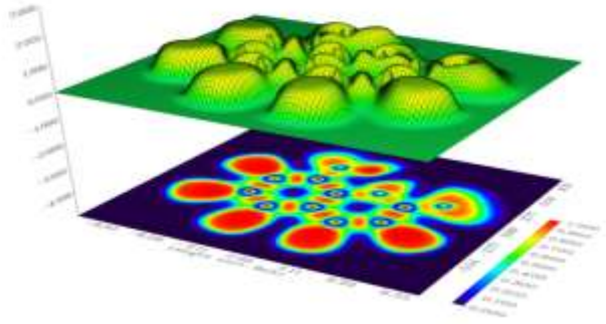

Fig. 11. ELF shade surface plot with projection of 8-OH coumarin.

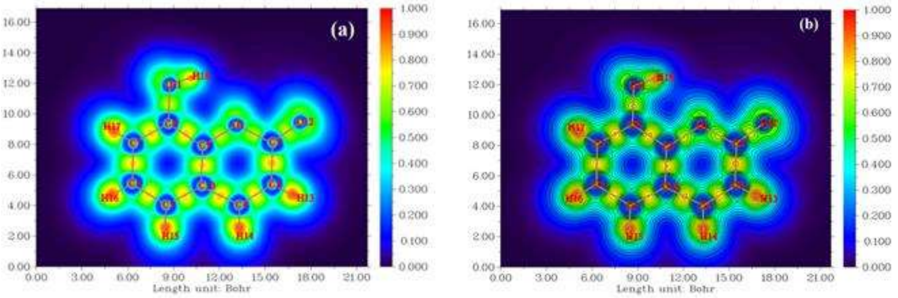

Fig. 12. (a) LOL colour shade diagram and (b) LOL contour map of 8-OH coumarin.

3.10. *Density of states and partial density of states analysis*

The DOS plots of the title compound are generated using Multiwfn software [22] (Fig. 13). In these graphical representations, the total density of states (TDOS) is shown in black, while the contributions from oxygen, carbon, and hydrogen atoms are represented by red, blue, and pink curves respectively. The overlapping density of states (OPDOS) of the molecule is plotted in green. Notably, the band gap value determined from the DOS analysis matches closely with that obtained from HOMO-LUMO analysis. The vertical dotted black line marks the position of the HOMO. A positive OPDOS value suggests bonding interactions, while a negative value indicates antibonding interactions and zero values denote non-bonding interactions. So, the OPDOS plot clearly highlights the presence of bonding, non-bonding, and antibonding interactions within the title compound.

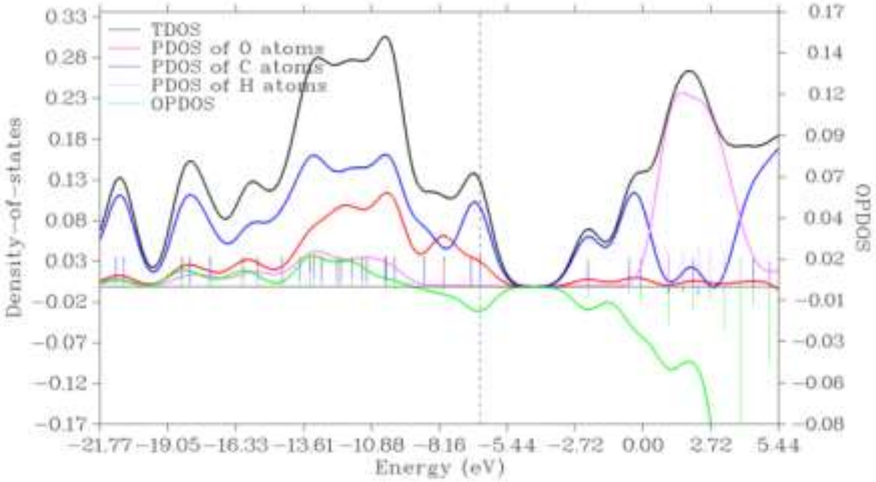

Fig. 13. Density of States plot with TDOS, PDOS, and OPDOS.

3.11. *Nonlinear optical properties*

Several nonlinear optical properties, like dipole moment (μ), polarizability (α) and first static hyperpolarizability (β) have been calculated by B3LYP/6-311++G(d,p) method. The calculation procedure has been described in detail previously [39].

Table 10. Calculated values of dipole moment, polarisability and first hyperpolarizability of 8-OH coumarin.

Parameters	Values	Parameters	Values	Parameters	Values
μ_x	-0.959340	α_{xx}	170.90400	β_{xxx}	-228.84800
μ_y	-1.406199	α_{xy}	5.65632	β_{xxy}	120.18700
μ_z	-0.000079	α_{yy}	122.68600	β_{xyy}	10.59450
μ	1.702272	α_{xz}	0.00339	β_{yyy}	243.10700
		α_{yz}	-0.00138	β_{xxz}	0.01240
		α_{zz}	58.63040	β_{xyz}	0.00593
		$\alpha_0(\mathrm{a.u.})$	117.40680	β_{yyz}	0.00858
		$\alpha_0(\mathrm{e.s.u.})$	1.740×10^{-23}	β_{xzz}	63.41780
				β_{yzz}	76.04500
				β_{zzz}	0.00925
				β_x	-154.83570

β_y	439.33900
β_z	0.03023
β_0(a.u.)	465.82492
β_0(e.s.u.)	4.0244×10^{-30}

In nonlinear optical studies, urea is widely used as a benchmark reference material for comparison with organic systems. The β_0 value of urea is 0.3728×10^{-30} e.s.u. [40], whereas that of 8-OH coumarin is 4.0244×10^{-30} e.s.u. which is approximately eleven times higher than that of urea. This indicates that 8-OH coumarin exhibits significantly stronger nonlinear optical activity. This enhanced behaviour is likely due to the extensive electron delocalization along the bond axes within the molecule.

Table 11 shows that among the first hyperpolarizability tensor components, β_{yyy} has the highest value. This indicates that maximum electron delocalization occurs along this direction. Presumably this delocalization involves the movement of the π electron cloud from the donor to the acceptor and thereby polarizes the molecule and facilitates intramolecular charge transfer within the molecule.

3.12. *Noncovalent interactions*

Weak noncovalent interactions were examined using the Reduced Density Gradient (RDG) method [41]. The cube file and RDG were obtained through Multiwfn [22], while the iso-surface visualization was carried out using VMD [42]. The RDG versus sign(λ_2)ρ (a.u.) plot of the title compound is displayed in Fig. 14a. Each point in these graphs corresponds to a grid point in 3D space. The RDG plot shows several spikes. These spikes are classified into three main categories. The spikes in the negative region of the X axis i.e. sign$(\lambda_2)\rho$ $(a.u.)$ represent the hydrogen bonds, spikes in the middle represent the van der Waals interactions and spikes in the positive region represent the repulsive interactions [43].

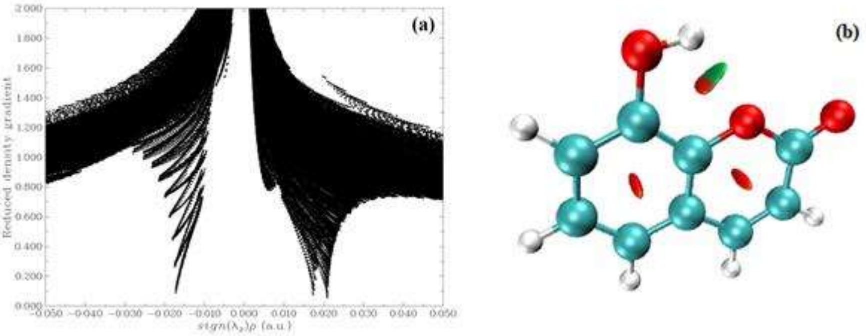

Fig. 14. (a) Plot of RDG versus sign $(\lambda_2)\rho$ $(a.u.)$ and (b) RDG isosurface plot of 8-OH coumarin.

Visualization of weak interactions is facilitated by RDG isosurface mapping, where color coding helps distinguish the nature of interactions. The RDG isosurface of the title molecule at an isovalue of 0.5 is displayed in Fig. 14b, with blue regions denoting hydrogen bonding, green indicating van der Waals interactions, and red corresponding to steric effects. From Fig. 14b, it is evident that the compound lacks intramolecular hydrogen bonds. Nonetheless, the hydroxyl hydrogen atom engages in a weak van der Waals interaction with the oxygen atom of the ring. Moreover, two steric interactions, though weak, are identified within the aromatic rings.

4. Conclusion

A detailed theoretical investigation of 8-hydroxy coumarin was conducted to elucidate its geometrical, spectroscopic, and electronic characteristics. Geometrical analysis demonstrated the influence of carbonyl and hydroxyl substituents on bond parameters, consistent with Laplacian electron density ($\nabla^2\rho$) topology results. NBO analysis revealed several conjugative and hyperconjugative interactions contributing to molecular stability. TD-DFT calculations identified a HOMO–LUMO gap of 4.32 eV, while the simulated UV spectrum displayed strong absorption peaks at 220 and 289 nm with a weak shoulder between 215–240 nm, corresponding to well-assigned vertical transitions. Simulated IR and NMR spectra provided reliable spectroscopic insights, with a high correlation ($R^2 = 0.99065$) confirming strong agreement with experimental NMR data. Frontier orbital analysis enabled the evaluation of reactivity descriptors, while ELF, LOL and DOS studies clarified the bonding, nonbonding, and antibonding interactions. Fukui functions and CDD analysis highlighted sites susceptible to electrophilic and nucleophilic attack. NLO calculations indicated notable nonlinear optical response and RDG analysis confirmed the absence of intramolecular hydrogen bonding but revealed weak van der Waals and steric interactions. Overall, this work not only validates experimental findings but also establishes a theoretical framework that may guide the design of coumarin-based molecules for applications in drug discovery, photophysics and nonlinear optical materials.

Acknowledgment

The author gratefully acknowledges and thanks I-STEM, Indian Institute of Science, Bengaluru-560012, Karnataka, India (I-STEM/Catalyticgrant/acad_23/2022-23) for a research grant.

References

1. M. J. Matos, L. Santana, E. Uriarte, O. A. Abreu, E. Molina, and E. G. Yordi, Coumarins — An Important Class of Phytochemicals, in: Phytochemicals - Isolation, Characterisation and Role in Human Health (2015). https://doi.org/10.5772/59982
2. C. Gnerre, M. Catto, F. Leonetti, P. Weber, P. A. Carrupt, C. Altomare, A. Carotti, and B. Testa, J. Med. Chem. **43**, 4747 (2000). https://doi.org/10.1021/JM001028O
3. N. S. A. Kader, H. Moustafa, A. L. El-Ansary, O. E. Sherif, and A. M. Farghaly, New J. Chem. **45**, 7714 (2021). https://doi.org/10.1039/D0NJ05688J
4. C. A. Kontogiorgis and D. J. Hadjipavlou-Litina, J. Med. Chem. **48**, 6400 (2005). https://doi.org/10.1021/jm0580149
5. A. M. Silván, M. J. Abad, P. Bermejo, M. Sollhuber, and A. Villar, J. Nat. Prod. **59**, 1183

(1996). https://doi.org/10.1021/NP960422F
6. C. A. Kontogiorgis and D. J. Hadjipavlou-Litina, Bioorg. Med. Chem. Lett. **14**, 611 (2004). https://doi.org/10.1016/J.BMCL.2003.11.060
7. G. Melagraki, A. Afantitis, O. Igglessi-Markopoulou, A. Detsi, M. Koufaki, C. Kontogiorgis, and D. J. Hadjipavlou-Litina, Eur. J. Med. Chem. **44**, 3020 (2009). https://doi.org/10.1016/j.ejmech.2008.12.027
8. C. Yoakim, P. R. Bonneau, R. Déziel, L. Doyon, J. Duan, I. Guse, S. Landry, E. Malenfant, J. Naud, W.W. Ogilvie, J. A. O'Meara, R. Plante, B. Simoneau, B. Thavonekham, M. Bös, and M. G. Cordingley, Bioorg. Med. Chem. Lett. **14**, 739 (2004). https://doi.org/10.1016/J.BMCL.2003.11.049
9. D. Yu, M. Suzuki, L. Xie, S. L. Morris-Natschke, and K. H. Lee, Med. Res. Rev. **23**, 322 (2003). https://doi.org/10.1002/med.10034
10. S. A. Patil, V. Kandathil, A. Sobha, S. B. Somappa, M. R. Feldman, A. Bugarin, and S. A. Patil, Molecules. **27**, 5220 (2022). https://doi.org/10.3390/molecules27165220
11. R. A. O'reilly, P. M. Aggeler, and L. S. Leong, J. Clin. Invest. **42**, 1542 (1963). https://doi.org/10.1172/JCI104839
12. E. Aktoudianakis and A. P. Dicks, J. Chem. Educ. **83**, 287 (2006). https://doi.org/10.1021/ed083p287
13. T. Sugino and K. Tanaka, Chem. Lett. 110 (2001). https://doi.org/10.1246/CL.2001.110
14. S. Kumar, V. C. Rao, and R. C. Rastogi, Spectrochim. Acta - Part A Mol. Biomol. Spectrosc. **57**, 41 (2001). https://doi.org/10.1016/S1386-1425(00)00330-9
15. A. Carneiro, M. J. Matos, E. Uriarte, and L. Santana, Molecules **26**, 501 (2021). https://doi.org/10.3390/molecules26020501
16. A. Gaber, W. F. Alsanie, M. Alhomrani, A. S. Alamri, I. M. El-Deen, and M. S. Refat, Crystals **11**, 565 (2021). https://doi.org/10.3390/cryst11050565
17. H. Gümüş, J. Clin. Orthop. Trauma Care **6**, 1 (2024). https://doi.org/10.31579/2694-0248/098
18. D. Q. Huong, D. Van Truong, N. M. Tam, and P. C. Nam, J. Mol. Liq. **391**, ID 123312 (2023). https://doi.org/10.1016/j.molliq.2023.123312
19. D. Vijay, Y. S. Priya, M. Satyavani, A. K. Das, B. N. Rajasekhar, and A. Veeraiah, Spectrochim. Acta Part A Mol. Biomol. Spectrosc. **229**, ID 117930 (2020). https://doi.org/10.1016/j.saa.2019.117930
20. M. J. Frisch, G. W. Trucks, H. B. Schlegel, G. E. Scuseria, M. A. Robb et al., Gaussian–09, (Gaussian, Inc., Wallingford, CT, 2009). https://gaussian.com/g09citation/
21. A. Frisch, A. B. Nielsen, and A. J. Holder, Gauss View User Manual (Gaussian Inc., Pittsburg, PA, 2001).
22. T. Lu and F. Chen, J. Comput. Chem. **33**, 580 (2012). https://doi.org/10.1002/jcc.22885
23. M. H. Jamróz, Spectrochim. Acta - Part A Mol. Biomol. Spectrosc. **114**, 220 (2013). https://doi.org/10.1016/j.saa.2013.05.096
24. R. F. W. Bader, Atoms in Molecules: A Quantum Theory (Oxford University Press, Oxford, U.K, 1990).
25. R. F. W. Bader and H. Essén, J. Chem. Phys. **80**, 1943 (1983). https://doi.org/10.1063/1.446956
26. A. E. Reed, R. B. Weinstock, and F. Weinhold, J. Chem. Phys. **83**, 735 (1985). https://doi.org/10.1063/1.449486
27. G. Keresztury, S. Holly, G. Besenyei, J. Varga, A. Wang, and J. R. Durig, Spectrochim. Acta - Part A Mol. Spectrosc. **49A**, 2007 (1993).https://doi.org/10.1016/S0584-8539(09)91012-1
28. J. P. Foster and F. Weinhold, J. Am. Chem. Soc. **102**, 7211 (1980). https://doi.org/10.1021/ja00544a007
29. S. Khatua, J. Adv. Sci. Res. **12**, 304 (2021). https://doi.org/10.55218/JASR.s12021122sup115
30. A. M. Asiri, M. Karabacak, M. Kurt, and K.A. Alamry, Spectrochim. Acta - Part A Mol. Biomol. Spectrosc. **82**, 444 (2011). https://doi.org/10.1016/j.saa.2011.07.076
31. J. N. Liu, Z. R. Chen, and S. F. Yuan, J. Zhejiang Univ. Sci. **6 B**, 584 (2005). https://doi.org/10.1631/jzus.2005.B0584
32. H. Duddeck and M. Kaiser, Org. Magn. Reson. **20**, 55 (1982).

https://doi.org/10.1002/mrc.1270200202

33. A. J. D. Melinda, Solid State NMR Spectroscopy, Principles and Applications (Cambridge University Press, Cambridge, 2003).
34. F. X. W. R. M. Silverstein, Spectrometric Identification of Organic Compounds, 6th Edition (J. Wiley and Sons, Chichester, 2004).
35. A. D. Becke and K. E. Edgecombe, J. Chem. Phys. **92**, 5397 (1990). https://doi.org/10.1063/1.458517
36. B. Silvi and A. Savin, Nature **371**, 683 (1994). https://doi.org/10.1038/371683a0
37. S. Sarala, S. K. Geetha, S. Muthu, and A. Irfan, J. Mol. Model. **27**, 266 (2021). https://doi.org/10.1007/s00894-021-04877-z
38. B. F. Rizwana, J. C. Prasana, S. Muthu, and C. S. Abraham, Comput. Biol. Chem. **78**, 9 (2019). https://doi.org/10.1016/j.compbiolchem.2018.11.014
39. K. S. Thanthiriwatte and K. M. N. de Silva, J. Mol. Struct. THEOCHEM. **617**, 169 (2002). https://doi.org/10.1016/S0166-1280(02)00419-0
40. C. Adant, M. Dupuis, and J. L. Bredas, Int. J. Quantum Chem. **56**, 497 (1995). https://doi.org/10.1002/qua.560560853
41. E. R. Johnson, S. Keinan, P. Mori-Sánchez, J. Contreras-García, A. J. Cohen, and W. Yang, J. Am. Chem. Soc. **132**, 6498 (2010). https://doi.org/10.1021/ja100936w
42. W. Humphrey, A. Dalke, and K. Schulten, J. Mol. Graph. **14**, 33 (1996). https://doi.org/10.1016/0263-7855(96)00018-5
43. B. S. Shyamala, P. V. A. Lakshmi, and V. J. Raju, J. Sci. Res. **2**, 525 (2010). https://doi.org/10.3329/jsr.v2i2.4673